Check for updates

Advanced Healthcare Materials

ADVANCED HEALTHCARE MATERIALS
www.advhealthmat.de

RESEARCH ARTICLE OPEN ACCESS

Molecular Design of Highly Efficient Heavy-Atom-Free Near-Infrared Cyanine Photosensitizers for Fluorescence Image-Guided Photodynamic Therapy of Solid Tumors

Van-Nghia Nguyen[1,#] | Huixian Liang[2,#] | Hyunsun Jeong[3,#] | Jieun Bang[3,#] | Chang Woo Koh[4] | Kunemadihali Mathada Kotraiah Swamy[3] | Sungnam Park[4] | JaeHong Park[3,5] | Fabiao Yu[2] | Juyoung Yoon[3,6]

[1]School of Chemistry and Life Sciences, Hanoi University of Science and Technology, Hanoi, Vietnam | [2]Key Laboratory of Emergency and Trauma, Key Laboratory of Haikou Trauma, Key Laboratory of Hainan Trauma and Disaster Rescue, Ministry of Education, The First Affiliated Hospital, Hainan Medical University, Haikou, China | [3]Department of Chemistry and Nanoscience, Ewha Womans University, Seoul, Republic of Korea | [4]Department of Chemistry, Korea University, Seoul, Republic of Korea | [5]Institute of Multiscale Matter and Systems (IMMS), Ewha Womans University, Seoul, Republic of Korea | [6]Graduate Program in Innovative Biomaterials Convergence, Ewha Womans University, Seoul, Republic of Korea

Correspondence: Van-Nghia Nguyen (nghia.nguyenvan@hust.edu.vn) | JaeHong Park (jaehong@ewha.ac.kr) | Fabiao Yu (yufabiao@muhn.edu.cn) | Juyoung Yoon (jyoon@ewha.ac.kr)

Received: 14 November 2025 | **Revised:** 16 January 2026 | **Accepted:** 24 January 2026

Keywords: NIR photosensitizer | cancer therapy | fluorescence imaging | photodynamic therapy | type I PDT

ABSTRACT

Recent advancements in photodynamic therapy (PDT) have highlighted its potential as a non-invasive cancer treatment. However, to fully realize the clinical potential of PDT, the development of innovative photosensitizers is essential. In this study, efficient heavy-atom-free PSs (IR820-1–3) activated by 808 nm light irradiation were developed by incorporating electron-rich/sterically bulky groups at the meso-position of the IR820 scaffold, a novel indocyanine green derivative. Notably, experimental results and transient absorption spectroscopic studies indicated that substituent bulkiness plays a key role in promoting reactive oxygen species (ROS) generation. IR820-3 PS, with a highly twisted molecular structure, demonstrated superior ROS production via both type I and type II photochemical pathways. The self-assembled nanostructure of IR820-3 underwent partial disassembly upon interaction with albumin, resulting in enhanced fluorescence intensity and photodynamic efficiency. Interestingly, the cationic cyanine backbone facilitated the mitochondria-specific localization of IR820-3, which further contributed to IR820-3's effective PDT performance against cancer cells. Importantly, in vivo findings indicated that the IR820-3 exhibited excellent tumor-targeting ability and induced efficient tumor photoablation under 808 nm NIR irradiation. This study provides insights into the molecular design of a facile, "one-for-all" NIR photosensitizer based on a heptamethine cyanine platform, highlighting its potential for preclinical and clinical applications.

1 | Introduction

Theranostic technology, which combines both diagnosis and therapy, has garnered significant attention in recent years, particularly in the context of precision medicine [1, 2]. Fluorescence image-guided photodynamic therapy (PDT) has emerged as a promising modality for cancer treatment due to its non-invasive nature, high therapeutic efficacy, and minimal side effects [3–6]. The photosensitizer (PS), a key component of PDT, can either be synthetically developed or naturally derived. Upon exposure

[#]These authors contributed equally to this work.

This is an open access article under the terms of the Creative Commons Attribution-NonCommercial License, which permits use, distribution and reproduction in any medium, provided the original work is properly cited and is not used for commercial purposes.
© 2026 The Author(s). *Advanced Healthcare Materials* published by Wiley-VCH GmbH

to light of an appropriate wavelength, the PS reaches an excited state and emits fluorescence as it relaxes from the singlet excited state (S_1) to the ground state (S_0). This fluorescence can be used for applications such as fluorescence-based diagnosis, real-time monitoring of drug distribution, and assessment of therapeutic responses in living systems [3, 7]. Beyond fluorescence emission, PSs can transfer energy from the triplet excited state (T_1) to nearby molecules, generating reactive oxygen species (ROS), such as singlet oxygen (via energy transfer from T_1 to oxygen; type II PDT) or free radicals (via electron transfer from T_1 to biological substrates; type I PDT), which can induce the selective destruction of cancer cells and tumor tissues [8–10]. However, the clinical efficacy of type II PDT for solid tumors is limited by both the hypoxic tumor microenvironment and the additional oxygen consumption during type II PDT, which further exacerbates the oxygen depletion [11–14]. As a result, recent studies have focused on type I PSs as a promising strategy to overcome the limitations of PDT under hypoxic conditions [12, 15–19].

To date, most of the clinically approved PSs used in PDT for cancer treatment are based on organic platforms; however, they suffer from poor water solubility, limited biocompatibility, and poor tumor selectivity. Although various nanoscale drug delivery systems have been developed to overcome these shortcomings, such strategies often require multiple components, non-biodegradable materials, and time-consuming, multistep fabrication methods. Moreover, the low reagent loading efficiency and potential toxicity of these "all-in-one" systems further hinder clinical translation [20–22]. Therefore, the development of single-component theranostic agents that integrate both fluorescence imaging and PDT functionality is highly desirable [21, 23]. Additionally, current PSs with short-wavelength absorption and emission (typically below 680 nm) often face limitations in biological applications due to the strong absorption of endogenous fluorophores in that wavelength range [24]. The development of near-infrared (NIR) PSs, particularly those with a maximum absorption wavelength above 700 nm, is crucial for achieving deep tissue penetration, reducing autofluorescence, and minimizing side effects, thereby contributing to effective in vivo theranostics [25, 26]. Furthermore, NIR light is less cytotoxic than ultraviolet (UV) or visible (vis) light, reducing potential adverse effects such as photodamage and skin photosensitization [27].

In recent years, heptamethine cyanine dyes have emerged as promising NIR fluorescent agents for tumor imaging, diagnosis, and therapy. A notable example is indocyanine green (ICG), which is approved by the Food and Drug Administration (FDA) and widely used in clinical settings [28, 29]. These cyanine dyes exhibit strong absorption and fluorescence in the first NIR window (NIR-I; 700–900 nm), allowing for deep tissue penetration, facile synthesis, and excellent biocompatibility [30–32]. Additionally, their intrinsic cationic nature enhances mitochondrial targeting [33, 34]. In particular, these dyes have a strong affinity for human serum albumin (HSA), forming stable noncovalent complexes upon binding [35]. These complexes tend to accumulate in tumors during biological applications [32]. Despite the progress made with cyanine-based PSs, several challenges remain, including poor stability, low targeting specificity, and suboptimal ROS quantum yields [36, 37]. A common approach to enhance ROS generation involves incorporating heavy atoms into the PS structure to promote intersystem crossing. However, this modification often leads to increased dark cytotoxicity, reduced fluorescence intensity, and shortened triplet state lifetimes, impeding clinical translation [6, 14, 37, 38]. Moreover, deactivation caused by the trans-to-cis rotation in the polyene chain remains a major concern [39].

This study introduces a simple molecular design strategy to develop highly efficient heptamethine cyanine PSs, which retain the unique optical properties of an ICG derivative, IR820, while overcoming the challenges outlined above. The resulting PSs offer several advantages: 1) incorporating sterically bulky substituents at the *meso*-position of the IR820 framework enhances ROS production under 808 nm irradiation; 2) these PSs generate significant ROS via both type I and type II photochemical pathways, making them effective for hypoxic tumors; 3) excitation and emission wavelengths around 808 nm support high signal-to-noise fluorescence imaging and effective treatment of deep-seated tumors; 4) In aqueous media, IR820-3 self-assembles into NanoIR820-3, which disassembles upon interaction with albumin, allowing switchable photoactivity; 5) this strategy provides a foundation for the future development of a "one-for-all" NIR PS in cancer therapy.

2 | Results and Discussion

2.1 | Molecular Design, Synthesis, Characterization, and Photophysical Properties of IR820-based PSs

Recently, heavy-atom-free cyanine PSs for cancer PDT have been developed. These PSs are constructed by introducing sterically bulky, electron-rich, or electron-withdrawing groups at the *meso*-position of the pentamethine cyanine (Cy5) skeleton [37, 39–41]. However, their relatively short excitation wavelengths (< 700 nm) restrict their use in high-resolution fluorescence imaging and deep tissue penetration. Moreover, the relationship between the steric/electronic properties of substituents and ROS generation remains unclear, and the dominance of type II ROS generation still hampers the broad applicability of these PSs [39]. The introduction of a sterically bulky substituent at the *meso*-position of the heptamethine cyanine (IR820) framework has been shown to enhance ROS generation through both type I and type II pathways under light and ultrasound activation [42]. However, a comprehensive investigation of the role of these substituents has been lacking, impeding the development of more efficient heptamethine cyanine-based PSs.

In this study, we designed and synthesized a series of heptamethine cyanine-based PSs by incorporating different electron-donating/sterically bulky moieties [triphenylamine, 4-methoxy-N-(4-methoxyphenyl)-N-phenylaniline, and 1,1,2,2-tetraphenylethene (TPE)] to the *meso*-position of the IR820 core for cancer PDT. IR820 was selected as the heptamethine cyanine backbone based on its promising properties, including a high molar extinction coefficient (> 10^5 M^{-1} cm^{-1}) in the NIR region and good photo- and chemical stability. This unique feature is derived from its structural similarity to ICG, along with improvements that enhance its chemical properties and photostability and allow further functionalization via chlorine-reactive sites [43, 44]. The goal of this study was to systematically

21922659, 2026, 15, Downloaded from https://advanced.onlinelibrary.wiley.com/doi/10.1002/adhm.202505692 by Ewha Womans University Library, Wiley Online Library on [28/09/2026]. See the Terms and Conditions (https://onlinelibrary.wiley.com/terms-and-conditions) on Wiley Online Library for rules of use; OA articles are governed by the applicable Creative Commons License

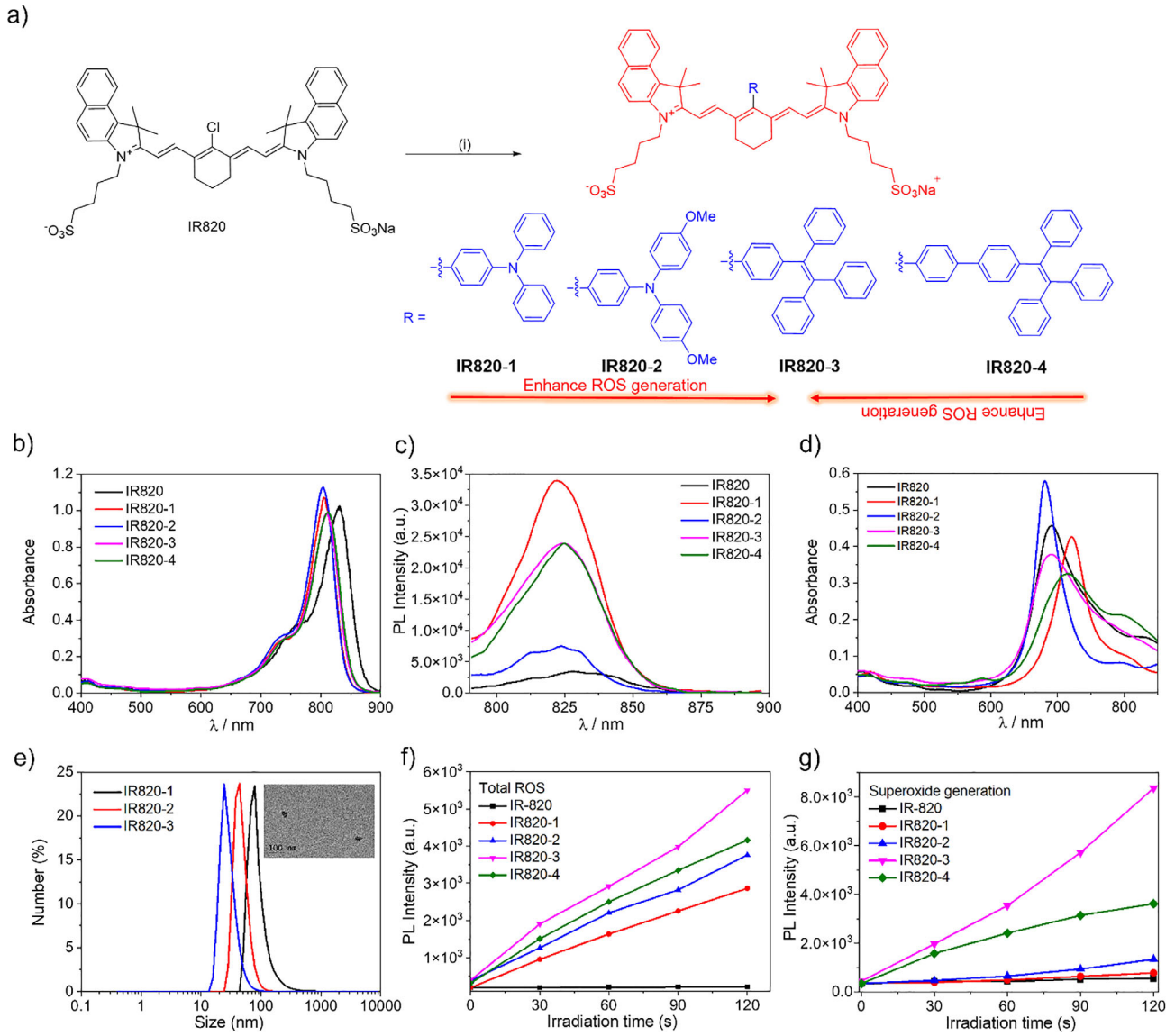


FIGURE 1 | (a) Chemical structures and synthetic route of IR820-based PSs. Reaction conditions: (i) R-boronic acid, K_2CO_3, $Pd(PPh_3)_4$, toluene/EtOH/water, reflux, overnight. (b) UV-vis absorption and (c) PL spectra of IR820 derivatives in DMSO (5 μM, λ_{ex} = 780 nm). (d) UV–vis absorption spectra of IR820 derivatives in PBS (5 μM). (e) Size distribution of IR820 derivatives in water (5 μM) detected by DLS; inset: morphology of IR820-3 determined by transmission electron microscopy. (f) Total ROS and (g) superoxide generation by IR820-based PSs in PBS (5 μM) upon 808 nm laser irradiation (0.3 W/cm^2).

investigate how the incorporation of different substituents at the *meso*-position influences the PDT efficacy of the resulting PSs and to develop efficient NIR PSs suitable for treating deep-seated tumors. A series of PSs (IR820-1–3) was synthesized via a one-step reaction (Figure 1a). For comparison, IR820-4, which contains 4-(1,2,2-triphenylvinyl)-1,1'-biphenyl (TPE-Ph) as a substituent, was also synthesized following previously reported methods [42]. All chemical structures were confirmed by ^{1}H NMR, ^{13}C NMR, and mass spectrometry (Figures S1–S7). The UV−vis absorption and fluorescence spectra of the IR820 derivatives in their monomeric state were measured in dimethyl sulfoxide (DMSO) (Table S1). All IR820 derivatives (IR820-1–3) exhibited strong UV−vis absorption bands around 812 nm, with molar extinction coefficients comparable to that of IR820 (approximately 2 × 10^5 M^{-1} cm^{-1}), indicating that substituent introduction at the *meso*-position preserved the excellent light-harvesting ability of the IR820 core (Figure 1b). The absorption spectra exhibited a slight blueshift as the electron-donating ability of the substituents increased. Density functional theory calculations revealed that this shift results from the electron-donating effects of the R groups, which elevate the energy level of the lowest unoccupied molecular orbital, with a minimal influence on the highest occupied molecular orbital (Figure S9). Moreover, all IR820 derivatives exhibited moderate fluorescence intensity, which is beneficial for fluorescence imaging applications (Figure 1c).

2.2 | ROS Generation by IR820-based PSs Under 808 Nm Light Irradiation

To evaluate triplet state formation and the potential of IR820 derivatives as effective PSs for PDT, ROS generation under NIR

21922659, 2026, 15, Downloaded from https://advanced.onlinelibrary.wiley.com/doi/10.1002/adhm.202505692 by Ewha Womans University Library, Wiley Online Library on [28/09/2026]. See the Terms and Conditions (https://onlinelibrary.wiley.com/terms-and-conditions) on Wiley Online Library for rules of use; OA articles are governed by the applicable Creative Commons License

irradiation was examined in phosphate-buffered saline (PBS). The aggregation behavior of IR820-based PSs in aqueous solution was first investigated by measuring their absorption and fluorescence spectra. In comparison with the corresponding monomers in DMSO, the absorption spectra of the IR820 dyes in PBS showed a significant decrease in intensity and a blue shift in the maximal absorption bands. This broadening of the spectra suggests the formation of H-aggregates (Figure 1d). Additionally, the fluorescence intensity was significantly reduced in PBS compared with DMSO (Figure S8). Dynamic light scattering (DLS) and transmission electron microscopy demonstrated the formation of spherical nanoparticles with an average size of approximately 30–80 nm in diameter (Figure 1e). These findings confirm the self-assembly of IR820 dyes into nanoparticles in aqueous solution. Notably, the nanostructures formed by IR820-3 and IR820-4 were more stable than those formed by IR820, owing to reduced π–π stacking interactions caused by their highly twisted structures [31].

Next, the ROS generation ability of the IR820-based PSs was evaluated using 2′, 7′-dichlorodihydrofluorescein diacetate (DCFH-DA) as a total ROS probe. As shown in Figure 1f, significantly more total ROS was generated by IR820-1–4 compared with the control IR820 under 808 nm laser irradiation (0.3 W/cm^2). Notably, IR820-3 demonstrated the highest ROS generation efficiency among the IR820-based PSs under identical conditions, with the order of ROS production being IR820-3> IR820-4> IR820-2> IR820-1> IR820. Although electron-donating groups have been reported to enhance ROS generation [39], our findings indicated that steric effects may be a key factor in ROS production [45]. Specifically, IR820-3 and IR820-4 generated substantial amounts of superoxide anion ($O_2^{\bullet-}$), as confirmed by dihydroethidium (DHE) assay (Figure 1g). In contrast, IR820, IR820-1, and IR820-2 generated minimal or no $O_2^{\bullet-}$ under the same laser irradiation (Figure 1g). We propose that the incorporation of sterically bulky TPE groups into the IR820 core induces highly twisted molecular structures, which inhibit isomerization, promote favorable self-assembly, and enhance ROS generation while reducing self-absorption [30, 31]. Overall, the findings highlight the potential of IR820-3 as a PS capable of generating ROS via both type I and type II pathways (Figure 1g and Figure S13a), which is particularly advantageous for PDT in hypoxic tumor environments.

2.3 | Ultrafast and Fast Transient Absorption Spectroscopy Experiments

To elucidate the origin of ROS generation, we examined the excited-state dynamics of IR820-based PSs using femtosecond transient absorption spectroscopy (fs-TAS) in N_2-saturated PBS. The transient absorption spectra for IR820 (Figure 2a), IR820-2 (Figure 2b), and IR820-3 (Figure 2c) were measured up to a delay time of 3600 ps. Negative spectral features between 650 and 900 nm, which corresponded to inverted steady-state absorption spectra (gray dashed lines), indicated ground-state depletion. Induced absorption (IA) bands from 500 to ~650 nm appeared immediately for all IR820-based PSs, assigned to the $S_1 \rightarrow S_n$ transition of the S_1 population [42]. IR820-2 and IR820-3 exhibited spectral evolution with the emergence of a new IA shoulder around 640 nm (Figure 2b,c, Figure S10b,c), starting at t_{delay} = 10 ps and becoming more pronounced at t_{delay} = 3600 ps. In contrast, IR820 showed no noticeable IA spectral evolution (Figure 2a and Figure S10a). The IA band at ~640 nm for IR820-2 and IR820-3 persisted beyond the instrumental temporal limit (t_{delay} = 3600 ps) and may be attributed to a triplet excited state. The findings were confirmed by nanosecond transient absorption spectroscopy (ns-TAS), which showed long-lived triplet state absorption.

To further investigate the effect of aggregation on triplet state formation and ROS generation, fs-TAS was performed in DMSO, where no aggregates were formed (Figure 1b). In DMSO, the fs-TAS spectra of IR820-based PSs (Figure S11a–c) showed no long-lived triplet state absorption (IA at ~640 nm). Isosbestic points appeared at 680 nm (IR820) and 670 nm (IR820-2 and IR820-3) between the IA bands of the S_1 state (500–680 nm or 670 nm) and the ground-state bleaching (GSB) bands, indicating that the S_1 population relaxes directly to the ground state. These results suggest that aggregation and structural distortion in aqueous environments are essential for facilitating triplet state formation.

Ns-TAS experiments confirmed the long-lived excited states of IR820-2 and IR820-3. Following photoexcitation, transient signals were observed at 680 nm (for IR820 and IR820-2) and 700 nm (for IR820-3), corresponding to the GSB bands of each IR820-based PS. Exponential fitting revealed GSB recovery time constants (τ_T) of 3.6 μs (Figure 2e) and 232 μs (Figure 2f) for IR820-2 and IR820-3, respectively, compared with < 0.1 μs for IR820 (Figure 2d). The sufficiently long τ_T (> 1 μs) under an N_2 atmosphere suggests that these long-lived excited states may originate from the triplet states of IR820-2 and IR820-3 [42]. Furthermore, the excited-state dynamics of IR820-based PSs indicated that the superior ROS generation of IR820-3 may be attributed to its extended triplet state lifetime, demonstrating that triplet state lifetime engineering can improve ROS generation efficiency [46, 47].

2.4 | ROS Generation by IR820-Based PSs Under 808 Nm Light Irradiation in the Presence of HSA

HSA, a highly abundant plasma protein, has recently been recognized as a versatile carrier for transporting various endogenous and exogenous substances [48, 49]. Given that albumin can encapsulate hydrophobic molecules [22, 23, 50], we explored the albumin-responsive properties of NanoIR820-3. The absorbance at ~812 nm, indicative of the monomeric form, increased with rising HSA concentrations (Figures 2g and Figure S12). In addition, concentration-dependent fluorescence enhancement was observed upon HSA addition (Figure 2h and Figure S12). The presence of HSA (2 eq) markedly enhanced ROS production by IR820-based PSs (Figure 1i,j and Figure S13b). DLS revealed that the average particle size of NanoIR820-3 decreased to approximately 6 nm after HSA addition, similar to the typical size of HSA (Figure 2k and Figure S14). This suggests that HSA encapsulated the IR820-3, inducing partial disassembly of NanoIR820-3. The observed enhancement in fluorescence intensity and ROS generation upon the addition of HSA may be attributed to the interaction between IR820-3 and the hydrophobic binding pocket of HSA, thereby suppressing quenching processes and excessive aggregation in aqueous solution [23, 51].

21922659, 2026, 15, Downloaded from https://advanced.onlinelibrary.wiley.com/doi/10.1002/adhm.202505692 by Ewha Womans University Library, Wiley Online Library on [28/09/2026]. See the Terms and Conditions (https://onlinelibrary.wiley.com/terms-and-conditions) on Wiley Online Library for rules of use; OA articles are governed by the applicable Creative Commons License

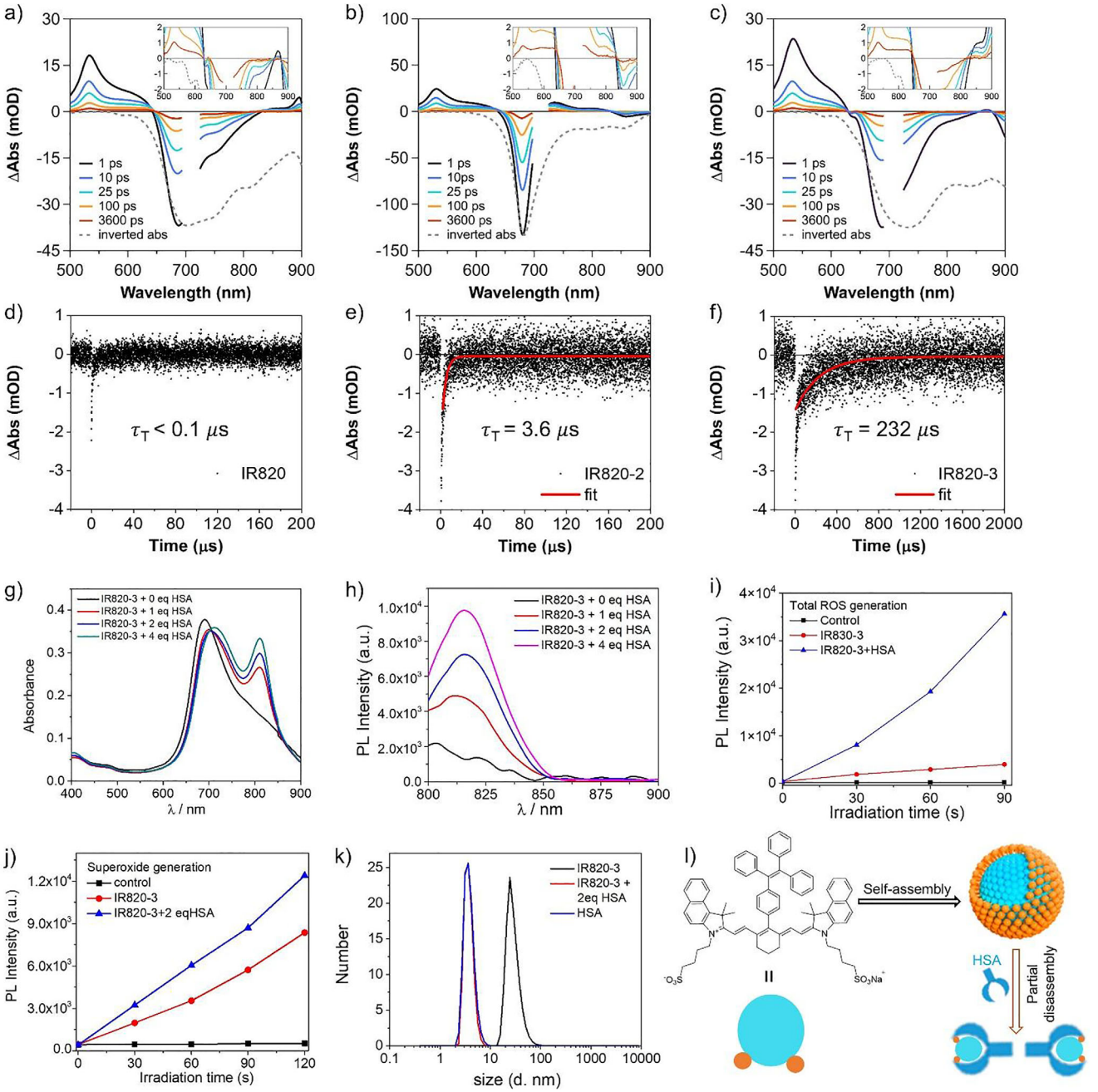


FIGURE 2 | Representative fs-TAS spectra of (a) IR820, (b) IR-820-2, and (c) IR820-3 in N_2-saturated PBS (λ_{ex} = 710 nm, ~0.26 μJ/pulse). Dashed grey lines indicate the inverted steady-state absorption spectra for comparison. ns-TAS transient decay signals of (d) IR820, (e) IR820-2, and (f) IR820-3 in N_2-saturated PBS. Experimental conditions for ns-TAS: (λ_{ex}: λ_{pr}) = (650 nm: 680 nm) for d) IR820 and e) IR820-2 and (680 nm: 700 nm) for f) IR820-3; excitation pulse energy = ~1 mJ/pulse. (g) UV–vis absorption and (h) fluorescence spectra of IR820-3 in water (5 μM) after HSA addition. Comparison of (i) total ROS and (j) superoxide generation of IR820-3 with/without HSA. (k) DLS size distribution of IR820-3 in water before and after HSA addition. (l) Schematic of the self-assembly and disassembly of IR820-3.

2.5 | In Vitro Experiments

Given their excellent photophysical and photochemical properties, we performed in vitro photoactivity experiments using HeLa cells. Initially, the cellular uptake of IR820-based PSs was assessed, which demonstrated the rapid accumulation of IR820-based PSs within HeLa cells within 30 min (Figure S16). Subsequently, we evaluated their intracellular distribution using a commercially available organelle-specific tracker. The red/NIR fluorescence of IR820-based PSs showed significant overlap with the green fluorescence of the mitochondrial MitoTracker Green probe (Figure 3a). The Pearson's correlation coefficients (Rr) for IR820, IR820-1, IR820-2, and IR820-3 were 0.80, 0.90, 0.95, and 0.81, respectively. Spectrally separated images of the two dyes were analyzed using Image-Pro Plus software. The intensity profiles of selected linear regions of interest, where HeLa cells were co-stained with the IR820 derivatives and MitoTracker (red arrow in Figure 3a), showed synchronous patterns. These results

21922659, 2026, 15, Downloaded from https://advanced.onlinelibrary.wiley.com/doi/10.1002/adhm.202505692 by Ewha Womans University Library, Wiley Online Library on [28/09/2026]. See the Terms and Conditions (https://onlinelibrary.wiley.com/terms-and-conditions) on Wiley Online Library for rules of use; OA articles are governed by the applicable Creative Commons License

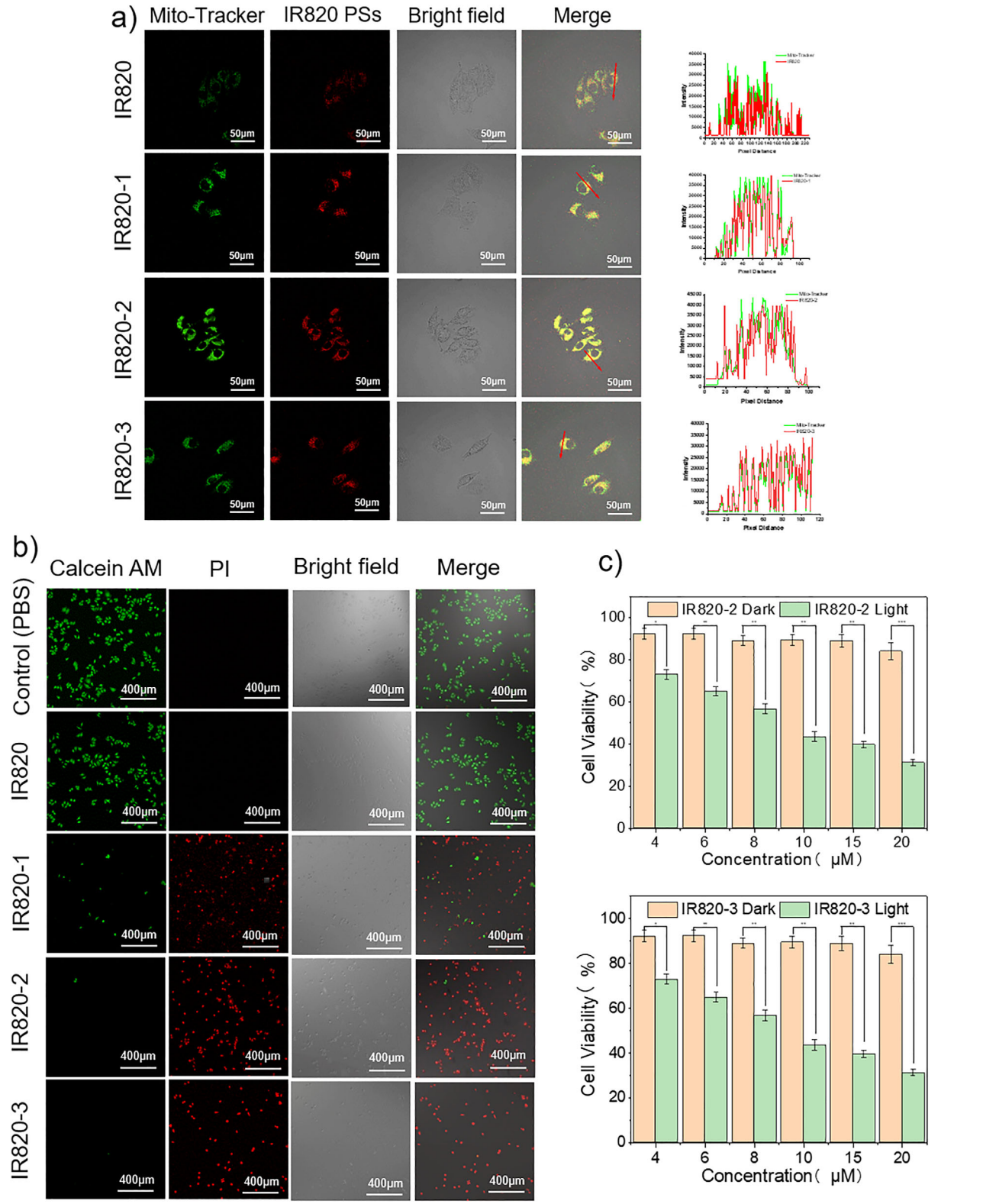


FIGURE 3 | A) Confocal fluorescence images of IR820-based PSs (10 μM) showing mitochondrial colocalization (MitoTracker: λ_{ex} = 488 nm, λ_{em} = 500−600 nm; scale: 50 μm). b) Confocal fluorescence images of calcein AM/PI-stained HeLa cells following IR820 (10 μM)-mediated photodamage (calcein AM: green channel, λ_{ex} = 488 nm, λ_{em} = 500−600 nm; PI: red channel, λ_{ex} = 545 nm, λ_{em} = 600−700 nm, 300 mW/cm^2, 15 min). c) Cell viability of HeLa cells after 30 min of incubation with IR820-1–3 under dark or light conditions (300 mW/cm^2, 15 min). Difference was analyzed by one-way ANOVA and Bonferroni post-test, ***$p < 0.001$.

21922659, 2026, 15, Downloaded from https://advanced.onlinelibrary.wiley.com/doi/10.1002/adhm.202505692 by Ewha Womans University Library, Wiley Online Library on [28/09/2026]. See the Terms and Conditions (https://onlinelibrary.wiley.com/terms-and-conditions) on Wiley Online Library for rules of use; OA articles are governed by the applicable Creative Commons License

indicate efficient internalization of the IR820 derivatives into the mitochondria, suggesting the role of the cationic structure in selective mitochondrial targeting.

Next, we assessed the in vitro biocompatibility and antitumor activity of IR820-based PSs. HeLa cells retained substantial viability after 6 h incubation with IR820-based PSs without laser irradiation (Figure S17). Notably, no concentration-dependent cytotoxic effects were observed, indicating high biocompatibility and minimal cytotoxicity under dark conditions. To determine the optimal conditions for PS-induced phototoxicity, we examined the effects of light exposure duration and laser power (Figures S18 and S19). After incubating the PSs with the cells for 30 min, a laser power of 300 mW/cm^2 was applied. Cell viability was evaluated by calcein AM/PI co-staining assay, which labels live and dead cells under varying illumination times. Additionally, we investigated the effect of laser power at a fixed illumination time of 15 min. The results showed that the highest PDT effect was achieved with IR820-based PSs when exposed to an 808 nm laser at 300 mW/cm^2 for 15 min. Under these optimal conditions, PBS and IR820 exerted minimal phototoxic effects on HeLa cells. In contrast, the phototoxic effects of IR820-1, IR820-2, and IR820-3 progressively increased from IR820-1 to IR820-3 (Figure 3b). Finally, we investigated the antitumor activity of IR820-1–3 PSs using CCK-8 assay. After exposure to 808 nm light, IR820-1–3 PSs effectively inhibited cancer cell proliferation in a concentration-dependent manner (Figure 3c and Figure S20). Among them, IR820-3 exhibited the highest PDT efficacy, inducing 72.0% cell death in HeLa cells. To validate the key hypothesis regarding the advantage of type-I PSs in overcoming hypoxia, it is necessary to quantitatively assess and compare the phototoxic effects of IR820-3 under strictly controlled normoxic and hypoxic environments, thereby verifying its efficacy in overcoming tumor hypoxia. As shown in Figure S21, the hypoxia group was treated under a predetermined low-oxygen environment (1% O_2). And the normoxia group was cultured under standard conditions (21% O_2). Following light exposure, we applied the MTT assay to quantitatively determine cell survival rates. There is no significant difference in the photodynamic killing efficacy of IR820-3 under hypoxic versus normoxic conditions. This experiment provides direct evidence to support that IR820-3 can effectively overcome hypoxia and maintain its photodynamic performance.

To elucidate the antitumor mechanism, intracellular levels of total ROS and superoxide anion production were assessed by confocal fluorescence imaging using specific ROS probes (DCFH-DA and DHE). All IR820-based PSs generated substantial amounts of ROS upon exposure to 808 nm laser irradiation (Figure 4). Among the tested PSs, IR820-3 showed the highest capacity for ROS generation. These observations are consistent with CCK-8 assay results, demonstrating that IR820-3 could exert high antitumor activity through type I and type II pathways. To further verify the intracellular cytotoxic mechanism of the mitochondria-targeting IR820-3 PS, we first utilized a mitochondria-localizing superoxide anion probe (Mito-Cy-Tfs, Figure S22) [52] and a mitochondria-localizing hydrogen peroxide probe (Mito-Bor, Figure S23) [53] to confirm the production and specifically the mitochondrial localization of these ROS upon light irradiation. Concurrently, to assess the consequent mitochondrial dysfunction, we measured the disruption of mitochondrial membrane potential ($\Delta\Psi_m$) using the fluorescent potentiometric dye JC-1. A decrease in the red/green fluorescence intensity ratio of JC-1 indicates the collapse of $\Delta\Psi_m$ (Figure S24), a pivotal early event in mitochondria-mediated apoptosis. In conclusion, our experimental findings confirm that IR820-3 functions as designed as a mitochondria-localizing photosensitizer that elicits its cytotoxic effect primarily through a Type I photochemical mechanism, which directly disrupts mitochondrial membrane potential and triggers cell death.

2.6 | In Vivo Experiments

To assess in vivo tumor accumulation of IR820-3, in vivo real-time fluorescence imaging of HeLa tumor-bearing mice was performed following intravenous (i.v.) administration of IR820-3. IR820-3 (100 μl, 10 μM) was injected into the tail vein of mice when the tumor reached about 100 mm^3. We observed an obvious fluorescence accumulation in the tumor via a small animal imaging system at different time intervals after injection. It was found that the fluorescence intensity of the tumor site gradually increased over time, reaching the maximum at 60 min, and then gradually decreased till 2 h (Figure 5a). To illustrate the change in fluorescence intensity more directly, the fluorescence of the tumor was quantitatively analyzed (Figure S25). This result indicates that IR820-3 could accumulate in tumors.

Encouraged by the the promising in vitro results and tumor accumulation of IR820-3, we evaluated its PDT effect on the tumor using HeLa tumor-bearing mice models. HeLa cells (2.5×10^6) were injected into the leg of each mouse to create tumor-bearing mice models. The mice were divided into five parallel groups. The five groups were treated with PBS, IR820, IR820-3, IR820 + laser, and IR820-3 + laser, respectively. When the tumor volume reached about 100 mm^3, the samples (100 μl, 10 μM) were injected through the tail vein of the tumor-bearing mice, respectively. The laser therapy groups were irradiated with an 808 nm laser (300 mW/cm^2, 15 min) for PDT treatment. At the first, fourth, ninth, and 14th day, the mice were photographed, and the tumor volume was measured to monitor the process of tumor development. The results displayed that the tumor in the IR820-3 + laser group was significantly reduced, while the tumor in other treatment groups was still significantly increased (Figure 5b). After 14 days, the mice were sacrificed, and the tumor samples were collected and weighed. The size and weight of tumor tissues from mice on day 14 after injection corresponded well with the results of tumor growth suppression (Figure 5c,d). The results reveal that the IR820-3 exhibited efficient inhibition of tumor growth under 808 nm light irradiation. Moreover, the weight of the mice was recorded every two days. The results revealed no significant weight fluctuations during the 14-day treatment period, demonstrating that the injected samples did not cause considerable systemic acute toxicity (Figure S26).

The efficacy and biocompatibility of each treatment group were verified at the microscopic level (Figure 6). Tumor lesions and major organs were collected and stained with hematoxylin and eosin for histological analysis (15 × objective). The results indicated significant apoptosis in tumors treated with IR820-3 + laser. In contrast, no distinct cellular damage was observed in the other groups. Furthermore, in the IR820-3-mediated PDT group, no evidence of necrosis or inflammatory damage was detected

21922659, 2026, 15, Downloaded from https://advanced.onlinelibrary.wiley.com/doi/10.1002/adhm.202505692 by Ewha Womans University Library, Wiley Online Library on [28/09/2026]. See the Terms and Conditions (https://onlinelibrary.wiley.com/terms-and-conditions) on Wiley Online Library for rules of use; OA articles are governed by the applicable Creative Commons License

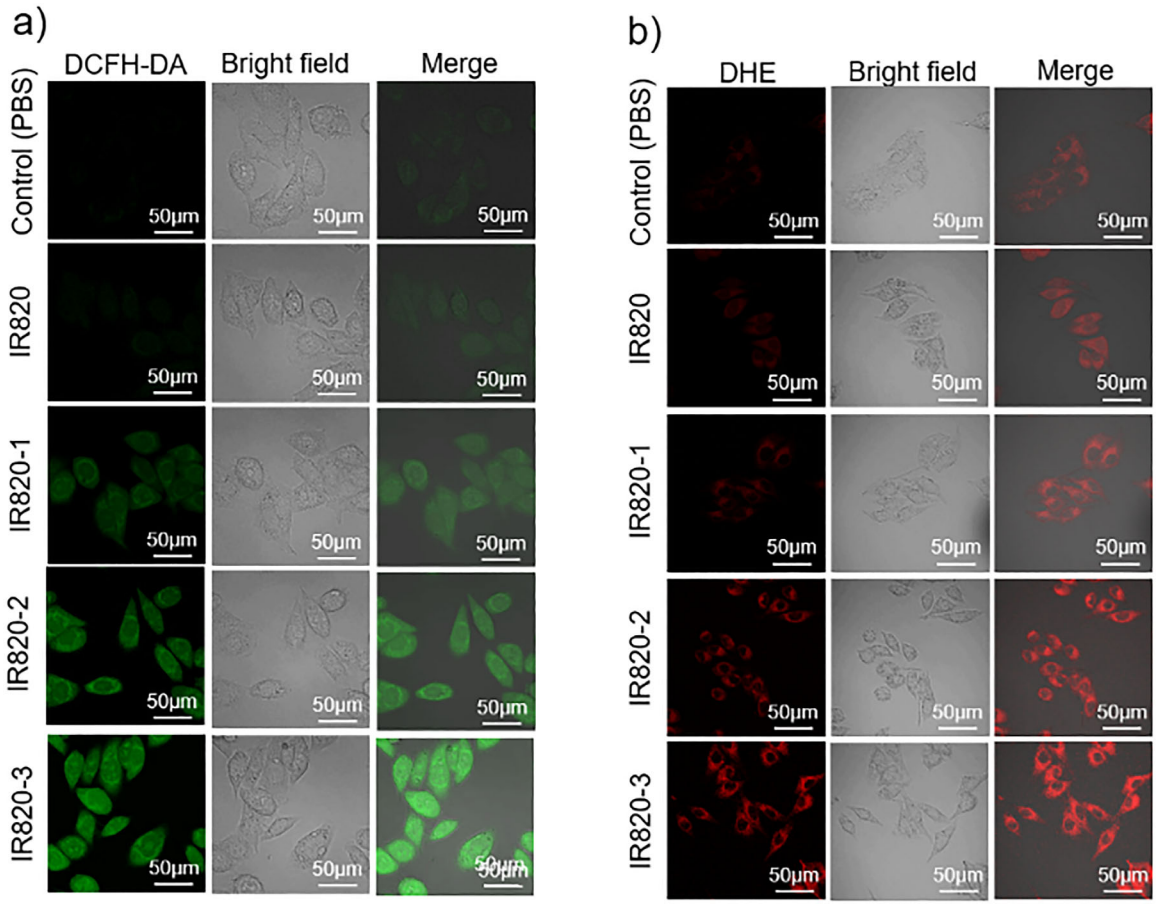


FIGURE 4 | Confocal fluorescence imaging of ROS generation in HeLa cells treated with IR820-based PSs (10 μM) under 808 nm laser irradiation (300 mW/cm^2, 15 min). a) Total ROS generation detected using the DCFH-DA probe (λ_{ex} = 488 nm, λ_{em} = 500–600 nm; scale: 50 μm). b) Superoxide anion generation detected using the DHE probe (λ_{ex} = 559 nm, λ_{em} = 575–675 nm; scale: 50 μm).

in major organs, including the heart, liver, spleen, lungs, and kidneys, suggesting the high biosafety of IR820-3. Overall, these results indicate effective tumor-targeting, high tumor inhibition efficacy, and excellent biosafety of IR820-3.

3 | Conclusion

We designed and developed highly efficient heavy-atom-free NIR PSs for enhanced fluorescence image-guided cancer PDT. By incorporating sterically bulky/electron-rich substituents at the *meso*-position of the IR820 framework, we gained new insights into the molecular design of heptamethine cyanine-based NIR PSs. The electron-donating ability and steric hindrance of these substituents are crucial for enhancing ROS production, with steric hindrance playing a particularly vital role. The findings were further supported by transient absorption spectroscopic studies. IR820-3, characterized by its highly twisted structure, exhibited the longest triplet state lifetime and superior ROS production through type I and type II photochemical mechanisms. The cationic backbone of the heptamethine cyanine framework allows for selective mitochondrial targeting, a key feature of the IR820-based PSs. Among the series of PSs (IR820-1–3), IR820-3 demonstrated the highest PDT efficacy, as well as moderate fluorescence imaging capability. In vivo results showed the accumulation of IR820-3 at the tumor sites after intravenous administration through the tail vein, resulting in efficient tumor inhibition. These findings suggest the potential of IR820-3 as a multifunctional PS for image-guided PDT, with prospects for preclinical and clinical applications. Furthermore, this study provides insights into the molecular design of versatile, "one-for-all" NIR PSs for cancer PDT.

4 | Experimental Section

4.1 | Synthesis of IR820-1

IR820 (300 mg, 0.35 mmol) and (4-(diphenylamino)phenyl)boronic acid (143 mg, 0.49 mmol) were dissolved in mixed solvents of toluene/ethanol/water (60 mL, v/v/v = 24:24:12). K_2CO_3 (195 mg 1.41 mmol) was added, and N_2 was bubbled through the solution for 30 min. $Pd(PPh_3)_4$ (41 mg 0.035 mmol) was added. The mixture was refluxed under N_2 atmosphere overnight. After removal of the solvent under reduced pressure, the obtained residue was purified by column chromatography using DCM/MeOH (70:30) to get a green solid (0.17 g, 45.5%). ^{1}H NMR (DMSO): δ 8.01-7.96 (m, 6H), 7.70 (d, J = 8.9 Hz, 2H), 7.64 (t, J = 7.8 Hz, 2H), 7.45 (t, J = 7.5 Hz, 2H), 7.39-7.36 (m, 4H), 7.32-7.28 (m, 4H), 7.17 (t, J = 8.6 Hz, 6H), 7.12 (t, J = 7.4 Hz, 2H), 6.27 (d, J = 14.2 Hz, 2H), 4.22 (s, 4H), 2.68 (s, 4H), 2.50 (t, J = 7.3 Hz, 4H), 1.95-1.89 (m, 2H), 1.83-1.69 (m, 4H),

21922659, 2026, 15, Downloaded from https://advanced.onlinelibrary.wiley.com/doi/10.1002/adhm.202505692 by Ewha Womans University Library, Wiley Online Library on [28/09/2026]. See the Terms and Conditions (https://onlinelibrary.wiley.com/terms-and-conditions) on Wiley Online Library for rules of use; OA articles are governed by the applicable Creative Commons License

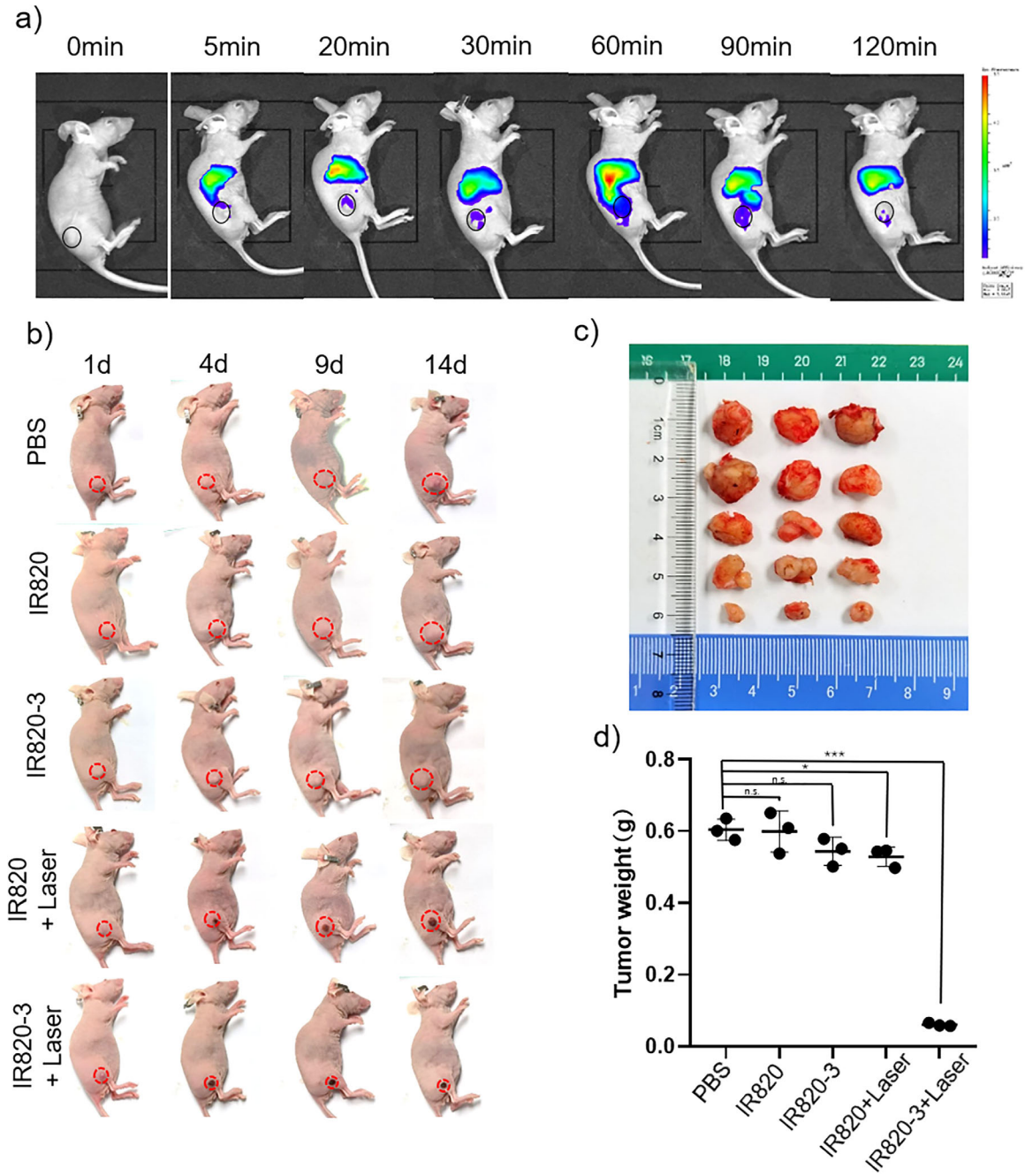


FIGURE 5 | a) In vivo biodistribution images from HeLa tumor-bearing mice after i.v. administration of IR820-3. b) Representative images of tumor-bearing mice at various time points after i.v. injection of various samples under 808 nm laser irradiation (300 mW/cm^2, 15 min). c) Representative images of tumors and d) tumor weights of the mice on day 14 after i.v. injection of various samples under 808 nm laser irradiation. Difference was analyzed by one-way ANOVA and Bonferroni post-test, ***$p < 0.001$.

1.75-1.69 (m, 4H), 1.46 (s, 12H). ^{13}C NMR (DMSO): δ 172.8, 161.1, 148.0, 147.6, 146.9, 140.5, 132.8, 131.8, 131.4, 139.9, 130.7, 130.0, 128.1, 127.8, 126.4, 125.2, 123.8, 123.7, 121.9, 112.3, 100.3, 51.3, 50.3, 44.0, 27.3, 26.8, 24.6, 23.0, 21.5. MALDI-TOF-MS calcd for $C_{64}H_{64}N_3O_6S$ $[M+2H]^+$; 1036.44, found: 1036.63.

4.2 | Synthesis of IR820-2

This compound was prepared in a manner analogous to the synthesis of IR820-1 using IR820, and (4-(bis(4-methoxyphenyl)amino) phenyl)boronic acid, IR820-2 was obtained as a green solid (48.9%). ^{1}H NMR (DMSO): *δ 8.11-8.04 (m, 6H), 7.75 (d, J* = 8.9 Hz, 2H), 7.68 (t, *J* = 7.2 Hz, 2H), 7.53-7.48 (m, 2H), 7.42 (d, *J* = 14.1 Hz, 2H), 7.21-7.17 (m, 8H), 7.05-7.00 (m, 4H), 6.31 (d, J = 14.2 Hz, 2H), 4.26 (s, 4H), 3.79 (s, 6H), 2.73 (s, 4H), 2.54-2.51 (m, 4H, overlap with DMSO peaks), 2.01-1.93 (m, 2H), 1.89-1.69 (8H), 1.56 (s, 12H). ^{13}C NMR (DMSO): δ 172.7, 161.6, 155.9, 148.8, 146.9, 141.2, 140.5, 132.8, 132.1, 131.7, 131.4, 131.1, 130.8, 130.6 128.0, 127.8, 126.0, 125.1, 123.2, 122.0, 115.3, 112.2, 100.2, 55.8, 51.2, 50.3, 27.2, 26.8, 23.0. MALDI-TOF-MS calcd for $C_{66}H_{68}N_3O_8S_2$ $[M+2H]^+$; 1096.46, found: 1096.67.

21922659, 2026, 15, Downloaded from https://advanced.onlinelibrary.wiley.com/doi/10.1002/adhm.202505692 by Ewha Womans University Library, Wiley Online Library on [28/09/2026]. See the Terms and Conditions (https://onlinelibrary.wiley.com/terms-and-conditions) on Wiley Online Library for rules of use; OA articles are governed by the applicable Creative Commons License

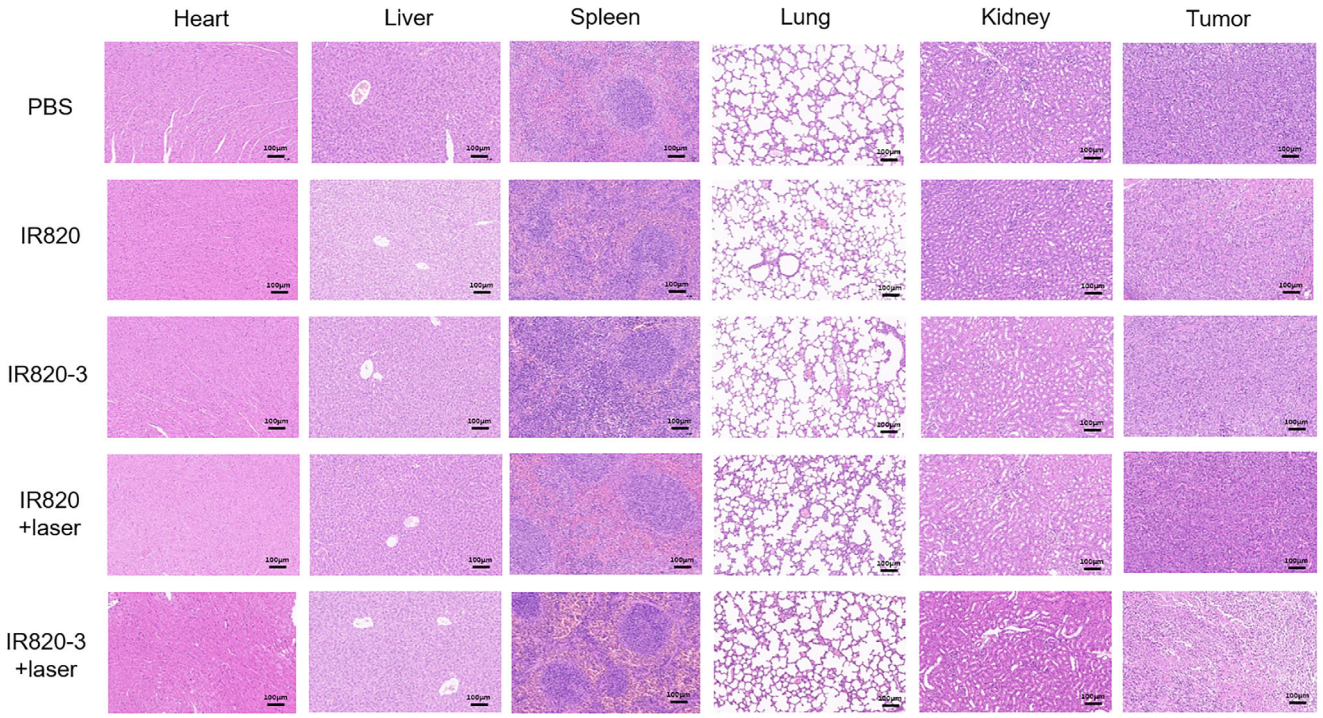


FIGURE 6 | H and E staining of tumor tissues and major organs of the tumor-bearing mice on day 14 after i.v. injection of various samples under irradiation with an 808 nm laser.

4.3 | Synthesis of IR820-3

This compound was prepared in a manner analogous to the synthesis of IR820-1 using IR820, and (4-(1,2,2-Triphenylvinyl)phenyl)boronic acid, IR820-3 was obtained as a green solid (48.9%). ^{1}H NMR (DMSO): δ 8.11 (d, J = 8.8 Hz, 2H), 8.06 (d, J = 8.6 Hz, 4H), 7.78-7.73(m,4H), 7.54-7.49 (m, 2H), 7.34-7.25 (m,12H), 7.21-7.08 (m, 8H), 6.28(d, J = 14.1 Hz, 2H), 4.26 (s, 4H), 2.72 (d, J = 9.1 Hz, 4H), 2.54 (s, 4H, overlap with DMSO peaks), 1.94 (s, 2H), 1.81-1.74 (m, 8H), 1.46 (s, 12H). ^{13}C NMR (DMSO): δ 172.4, 160.5, 145.7, 144.1, 143.8, 143.5, 141.1, 141.7, 140.4, 140.2, 136.8, 132.9, 131.7,131.6, 131.1, 131.0, 130.9, 130.8, 130.6, 129.8, 129.7, 128.3, 128.1, 128.0, 127.8, 127.2, 126.9, 125.1, 122.2, 112.2, 100.5, 52.1, 50.2, 27.2, 26.7, 23.0. MALDI-TOF-MS calcd for $C_{72}H_{69}N_2O_6S_2$ $[M+2H]^+$; 1123.48, found: 1124.03.

4.4 | Ultrafast and Fast Transient Absorption Spectroscopy Experiments

Femtosecond transient absorption (fs-TA) spectra were recorded using an ultrafast transient absorption spectrometer (HARPIA-TA, Light Conversion), consisting of a 6 kHz repetition rate femtosecond Yb:KGW amplifier laser (PHAROS, Light Conversion) and an optical parametric amplifier system (ORPHEUS, Light Conversion) in the National Research Facilities and Equipment Center (NanoBio-Energy Materials Center) at Ewha Womans University. Samples were prepared in 2 mm quartz cells.

Nanosecond transient absorption (ns-TA) data were acquired utilizing a home-built laser-flash photolysis system that consists of a 400–900 nm range continuous probe light from a halogen lamp, of which a detection wavelength was chosen with a monochromator (H10-UV, Horiba Jobin Yvon) interfaced with a PMT module (H10722-21 21P-01, Hamamatsu). Pump pulses were generated from a Nd:YAG-based broadband nanosecond laser system (NT340, EKSPLA, 20 Hz repetition rate), interfaced with an optical parametric oscillator (OPO), and the excitation pulse energy was adjusted to ~1.0 mJ/pulse. The change of probe signal intensity upon the photoexcitation was detected using a 500 MHz digital oscilloscope (TDS3052B, Tektronics). Samples were prepared in 1 cm quartz cells sealed with PTFE tape, rubber septa, and parafilm and purged with 99.99% N_2 gas before experiments.

4.5 | In Vitro experiments

For fluorescence imaging, 1×10^6 HeLa cells were taken and cultured in confocal dishes overnight, incubated with 10 μM PSs for 30 min, and photographed with FV3000.

For mitochondrial colocalization, 1×10^6 HeLa cells were taken and cultured in confocal dishes overnight, incubated with 10 μM PSs for 30 min incubated with 200 nM Mito-Tracker dye for 15 min, and photographed with FV3000.

For live and dead cell staining. 1×10^6 HeLa cells were taken and cultured in confocal dishes overnight, incubated with 10 μM PSs for 30 min, and irradiated in a xenon lamp light source system for 15 min (808 nm). Calcein AM/PI was added for 10 min staining, and photographs were taken photos by FV3000.

For cell viability assay, 5000 HeLa cells were taken and cultured in confocal dishes overnight, incubated with 10 μM PSs for 30 min

21922659, 2026, 15, Downloaded from https://advanced.onlinelibrary.wiley.com/doi/10.1002/adhm.202505692 by Ewha Womans University Library, Wiley Online Library on [28/09/2026]. See the Terms and Conditions (https://onlinelibrary.wiley.com/terms-and-conditions) on Wiley Online Library for rules of use; OA articles are governed by the applicable Creative Commons License

(irradiated with 808 nm laser for 15 min in the light group), and then determined with a cck-8 kit.

For reactive oxygen species assessment, 1×10^6 HeLa cells were taken and cultured in confocal dishes overnight, incubated with 10 μM PSs for 30 min, and irradiated with 808 nm laser for 15 min, adding 10 μM DCFH-DA (or 10 μM DHE) dye and stained for 10 min, and photographed with FV3000.

4.6 | In Vivo Experiments

Establishment of xenotrans plant cervical tumor model. All animal experiments were carried out in the animal experiment center of Hainan Medical University following the experimental protocol (HYLL-2022-358) approved by the Animal Protection Committee. Female Balb/c nude mice (18–20 g, 6–8 weeks) were used to establish the xenotrans plant cervical tumor model. In brief, the Balb/c mice were anesthetized with isoflurane gas in the absence of pathogens, and Hela cells 2.5×10^6 (100 μL) were injected into the right legs of each mouse to create a tumor-bearing mouse model. Tumor growth continued for 21 days.

4.7 | Statistical Analysis

Data from at least three independent experiments are expressed as mean ± standard deviation (SD). Statistical significance among groups was analyzed using one-way ANOVA followed by the Bonferroni post-test, with $^{***}p < 0.001$.

Acknowledgements

This research was funded by Hanoi University of Science and Technology (HUST) under project number T2024-XS-002. This research was supported by grants from the National Research Foundation of Korea (NRF), funded by the Korean government (MSIT and MOE) (Nos. RS-2024-00407093 for J.Y. and RS-2024-00397807, RS-2025-16063688 for J.P.), the National Natural Science Foundation of China (Nos. 22264013, 22305056, and 22164009), the Hainan Province Science and Technology Special Fund (ZDYF2022SHFZ311), the Hainan Province Clinical Medical Center (2021), and the Project for Functional Materials and Molecular Imaging Science Innovation Group of Hainan Medical University. We thank the Korea Basic Science Institute (Ochang) for help with the measurement of HRMS.

Conflicts of Interest

The authors declare no conflict of interest.

Data Availability Statement

The data that support the findings of this study are available in the supplementary material of this article.

References

1. R. Kumar, W. S. Shin, K. Sunwoo, et al., "Small Conjugate-Based Theranostic Agents: An Encouraging Approach for Cancer Therapy," *Chemical Society Reviews* 44 (2015): 6670–6683, https://doi.org/10.1039/C5CS00224A.

2. E. K. Lim, T. Kim, S. Paik, S. Haam, Y. M. Huh, and K. Lee, "Nanomaterials for Theranostics: Recent Advances and Future Challenges," *Chemical Reviews* 115 (2015): 327–394, https://doi.org/10.1021/cr300213b.

3. J. P. Celli, B. Q. Spring, I. Rizvi, et al., "Imaging and Photodynamic Therapy: Mechanisms, Monitoring, and Optimization," *Chemical Reviews* 110 (2010): 2795–2838, https://doi.org/10.1021/cr900300p.

4. J. Son, G. Yi, J. Yoo, C. Park, H. Koo, and H. S. Choi, "Light-responsive Nanomedicine for Biophotonic Imaging and Targeted Therapy," *Advanced Drug Delivery Reviews* 138 (2019): 133–147, https://doi.org/10.1016/j.addr.2018.10.002.

5. V. N. Nguyen, J. Ha, C. W. Koh, et al., "Access to the Triplet Excited States of Heavy-Atom-Free Boron-Dipyrromethene Photosensitizers via Radical Pair Intersystem Crossing for Image-Guided Tumor-Targeted Photodynamic Therapy," *Chemistry of Materials* 33 (2021): 7889–7896, https://doi.org/10.1021/acs.chemmater.1c02776.

6. V. N. Nguyen, Y. Yim, S. Kim, et al., "Molecular Design of Highly Efficient Heavy-Atom-Free Triplet BODIPY Derivatives for Photodynamic Therapy and Bioimaging," *Angewandte Chemie International Edition* 59 (2020): 8957–8962, https://doi.org/10.1002/anie.202002843.

7. Y. Y. Zhao, L. Lu, H. Jeong, et al., "Enhancing Biosafety in Photodynamic Therapy: Progress and Perspectives," *Chemical Society Reviews* 54 (2025): 7749–7768, https://doi.org/10.1039/D5CS00054H.

8. V. N. Nguyen, Y. Yan, J. Zhao, and J. Yoon, "Heavy-Atom-Free Photosensitizers: From Molecular Design to Applications in the Photodynamic Therapy of Cancer," *Accounts of Chemical Research* 54 (2021): 207–220, https://doi.org/10.1021/acs.accounts.0c00606.

9. T. C. Pham, V. N. Nguyen, Y. Choi, S. Lee, and J. Yoon, "Recent Strategies to Develop Innovative Photosensitizers for Enhanced Photodynamic Therapy," *Chemical Reviews* 121 (2021): 13454–13619, https://doi.org/10.1021/acs.chemrev.1c00381.

10. V. N. Nguyen, Z. Zhao, B. Z. Tang, and J. Yoon, "Organic Photosensitizers for Antimicrobial Phototherapy," *Chemical Society Reviews* 51 (2022): 3324–3340, https://doi.org/10.1039/D1CS00647A.

11. X. Zhao, J. Liu, J. Fan, H. Chao, and X. Peng, "Recent Progress in Photosensitizers for Overcoming the Challenges of Photodynamic Therapy: From Molecular Design to Application," *Chemical Society Reviews* 50 (2021): 4185–4219, https://doi.org/10.1039/D0CS00173B.

12. M. L. Li, T. Xiong, J. J. Du, et al., "Superoxide Radical Photogenerator with Amplification Effect: Surmounting the Achilles' Heels of Photodynamic Oncotherapy," *Journal of the American Chemical Society* 141 (2019): 2695–2702, https://doi.org/10.1021/jacs.8b13141.

13. X. Li, N. Kwon, T. Guo, Z. Liu, and J. Yoon, "Innovative Strategies for Hypoxic-Tumor Photodynamic Therapy," *Angewandte Chemie International Edition* 57 (2018): 11522–11531, https://doi.org/10.1002/anie.201805138.

14. X. Wang, X. Han, X. Tian, et al., "Regioisomeric Engineering of Sterically Hindered Bright Near-Infrared Paraptosis Agents for Chemo-Photodynamic Therapy," *Journal of the American Chemical Society* 147 (2025): 27068–27080, https://doi.org/10.1021/jacs.5c10005.

15. V. N. Nguyen, S. Qi, S. Kim, et al., "An Emerging Molecular Design Approach to Heavy-Atom-Free Photosensitizers for Enhanced Photodynamic Therapy Under Hypoxia," *Journal of the American Chemical Society* 141 (2019): 16243–16248, https://doi.org/10.1021/jacs.9b09220.

16. Y. Y. Zhao, L. Zhang, Z. Chen, et al., "Nanostructured Phthalocyanine Assemblies with Efficient Synergistic Effect of Type I Photoreaction and Photothermal Action to Overcome Tumor Hypoxia in Photodynamic Therapy," *Journal of the American Chemical Society* 143 (2021): 13980–13989, https://doi.org/10.1021/jacs.1c07479.

17. H. Shigemitsu, K. Ohkubo, K. Sato, et al., "Fluorescein-based type I Supramolecular Photosensitizer via Induction of Charge Separation by Self-Assembly," *JACS Au* 2 (2022): 1472–1478.

18. K. X. Teng, L. Y. Niu, and Q. Z. Yang, "Supramolecular Photosensitizer Enables Oxygen-Independent Generation of Hydroxyl Radicals for Pho-

21922659, 2026, 15, Downloaded from https://advanced.onlinelibrary.wiley.com/doi/10.1002/adhm.202505692 by Ewha Womans University Library, Wiley Online Library on [28/09/2026]. See the Terms and Conditions (https://onlinelibrary.wiley.com/terms-and-conditions) on Wiley Online Library for rules of use; OA articles are governed by the applicable Creative Commons License

todynamic Therapy," *Journal of the American Chemical Society* 145 (2023): 4081–4087, https://doi.org/10.1021/jacs.2c11868.

19. K. X. Teng, W. K. Chen, L. Y. Niu, W. H. Fang, G. Cui, and Q. Z. Yang, "BODIPY-based Photodynamic Agents for Exclusively Generating Superoxide Radical Over Singlet Oxygen," *Angewandte Chemie International Edition* 60 (2021).

20. E. Huynh and G. Zheng, "Engineering Multifunctional Nanoparticles: All-in-One Versus One-for-All," *WIREs Nanomedicine and Nanobiotechnology* 5 (2013): 250–265, https://doi.org/10.1002/wnan.1217.

21. X. Li, C. Y. Kim, S. Lee, et al., "Nanostructured Phthalocyanine Assemblies with Protein-Driven Switchable Photoactivities for Biophotonic Imaging and Therapy," *Journal of the American Chemical Society* 139 (2017): 10880–10886, https://doi.org/10.1021/jacs.7b05916.

22. H. B. Cheng, H. Dai, X. Tan, et al., "A Facile, Protein-Derived Supramolecular Theranostic Strategy for Multimodal-Imaging-Guided Photodynamic and Photothermal Immunotherapy In Vivo," *Advanced Materials* 34 (2022): 2109111, https://doi.org/10.1002/adma.202109111.

23. X. Li, S. Yu, Y. Lee, et al., "In Vivo Albumin Traps Photosensitizer Monomers from Self-Assembled Phthalocyanine Nanovesicles: A Facile and Switchable Theranostic Approach," *Journal of the American Chemical Society* 141 (2019): 1366–1372, https://doi.org/10.1021/jacs.8b12167.

24. G. He, M. He, R. Wang, et al., "Inside Back Cover: A Near-Infrared Light-Activated Photocage Based on a Ruthenium Complex for Cancer Phototherapy (Angew. Chem. Int. Ed. 24/2023)," *Angewandte Chemie International Edition* 62 (2023): 202218768.

25. B. Gu, W. Wu, G. Xu, et al., "Precise Two-Photon Photodynamic Therapy using an Efficient Photosensitizer With Aggregation-Induced Emission Characteristics," *Advanced Materials* 29 (2017): 1701076, https://doi.org/10.1002/adma.201701076.

26. G. Xu, C. Li, C. Chi, et al., "A supramolecular photosensitizer derived From an Arene-Ru(II) complex self-assembly for NIR activated photodynamic and photothermal therapy," *Nature Communications* 13 (2022): 3064, https://doi.org/10.1038/s41467-022-30721-w.

27. X. Li, S. Lee, and J. Yoon, "Supramolecular Photosensitizers Rejuvenate Photodynamic Therapy," *Chemical Society Reviews* 47 (2018): 1174–1188, https://doi.org/10.1039/C7CS00594F.

28. N. Kwon, G. O. Jasinevicius, G. Kassab, et al., "Nanostructure-Driven Indocyanine Green Dimerization Generates Ultra-Stable Phototheranostics Nanoparticles," *Angewandte Chemie International Edition* 62 (2023): 202305564, https://doi.org/10.1002/anie.202305564.

29. Z. M. Tao, G. S. Hong, C. Shinji, et al., "Biological Imaging Using Nanoparticles of Small Organic Molecules with Fluorescence Emission at Wavelengths Longer Than 1000 nm," *Angewandte Chemie International Edition* 52 (2013): 13002–13006, https://doi.org/10.1002/anie.201307346.

30. D. H. Li, C. L. Schreiber, and B. D. Smith, "Sterically Shielded Heptamethine Cyanine Dyes for Bioconjugation and High Performance Near-Infrared Fluorescence Imaging," *Angewandte Chemie International Edition* 59 (2020): 12154–12161, https://doi.org/10.1002/anie.202004449.

31. X. J. Zhao, H. J. Zhao, S. Wang, et al., "A Tumor-Targeting Near-Infrared Heptamethine Cyanine Photosensitizer with Twisted Molecular Structure for Enhanced Imaging-Guided Cancer Phototherapy," *Journal of the American Chemical Society* 143 (2021): 20828–20836, https://doi.org/10.1021/jacs.1c09155.

32. Y. Qiu, B. Yuan, Y. Cao, et al., "Recent Progress on Near-infrared Fluorescence Heptamethine Cyanine Dye-based Molecules and Nanoparticles for Tumor Imaging and Treatment," *Wiley Interdisciplinary Reviews: Nanomedicine and Nanobiotechnology* (2023): 1910.

33. S. L. Luo, X. Tan, S. T. Fang, et al., "Mitochondria-Targeted Small-Molecule Fluorophores for Dual Modal Cancer Phototherapy," *Advanced Functional Materials* 26 (2016): 2826–2835, https://doi.org/10.1002/adfm.201600159.

34. Y. Zou, M. L. Li, T. Xiong, et al., "A Single Molecule Drug Targeting Photosensitizer for Enhanced Breast Cancer Photothermal Therapy," *Small* 16 (2020): 1907677, https://doi.org/10.1002/smll.201907677.

35. X. Li, K. Jeong, Y. Lee, et al., "Water-Soluble Phthalocyanines Selectively Bind to Albumin Dimers: A Green Approach Toward Enhancing Tumor-Targeted Photodynamic Therapy," *Theranostics* 9 (2019): 6412–6423, https://doi.org/10.7150/thno.35210.

36. C. Zhang, L. Long, and C. M. Shi, "Mitochondria-Targeting IR-780 Dye and Its Derivatives: Synthesis, Mechanisms of Action, and Theranostic Applications," *Advanced Therapeutics* 1 (2018): 1800069, https://doi.org/10.1002/adtp.201800069.

37. H. Ma, Y. Lu, Z. B. Huang, et al., "ER-Targeting Cyanine Dye as an NIR Photoinducer to Efficiently Trigger Photoimmunogenic Cancer Cell Death," *Journal of the American Chemical Society* 144 (2022): 3477–3486, https://doi.org/10.1021/jacs.1c11886.

38. Z. Wang, L. Huang, Y. Yan, et al., "Elucidation of the Intersystem Crossing Mechanism in a Helical BODIPY for Low-Dose Photodynamic Therapy," *Angewandte Chemie International Edition* 59 (2020): 16114–16121, https://doi.org/10.1002/anie.202005269.

39. X. Zhao, Q. Yao, S. Long, et al., "An Approach to Developing Cyanines with Simultaneous Intersystem Crossing Enhancement and Excited-State Lifetime Elongation for Photodynamic Antitumor Metastasis," *Journal of the American Chemical Society* 143 (2021): 12345–12354, https://doi.org/10.1021/jacs.1c06275.

40. X. Z. Zhao, S. He, W. J. Chi, et al., *Advancement of Science* (2022): 9.

41. X. Zhao, S. He, J. Wang, et al., "Near-Infrared Self-Assembled Hydroxyl Radical Generator Based on Photoinduced Cascade Electron Transfer for Hypoxic Tumor Phototherapy," *Advanced Materials* 35 (2023): 2305163, https://doi.org/10.1002/adma.202305163.

42. V. N. Nguyen, T. G. Nguyen Cao, H. Jeong, et al., "Tumor-Targeted Exosome-Based Heavy Atom-Free Nanosensitizers with Long-Lived Excited States for Safe and Effective Sono-Photodynamic Therapy of Solid Tumors," *Advanced Healthcare Materials* 14 (2025): 2500927, https://doi.org/10.1002/adhm.202500927.

43. W. Pham, W. F. Lai, R. Weissleder, and C. H. Tung, "High Efficiency Synthesis of a Bioconjugatable Near-Infrared Fluorochrome," *Bioconjugate Chemistry* 14 (2003): 1048–1051, https://doi.org/10.1021/bc034070h.

44. I. Mohammad, C. Stanford, M. D. Morton, Q. Zhu, and M. B. Smith, "Structurally Modified Indocyanine Green Dyes. Modification of the Polyene Linker," *Dyes and Pigments* 99 (2013): 275–283, https://doi.org/10.1016/j.dyepig.2013.05.001.

45. X. Wang, X. Han, X. Tian, et al., "Regioisomeric Engineering of Sterically Hindered Bright Near-Infrared Paraptosis Agents for Chemo-Photodynamic Therapy," *Journal of the American Chemical Society* 147 (2025): 27068–27080, https://doi.org/10.1021/jacs.5c10005.

46. D. Lee, H. Sun, J. Bang, et al., "Dual-Enhanced Nanohybrids for Synergistic Photothermal and Photodynamic Therapy in Cancer Treatment With Immune Checkpoint Inhibitors," *Advanced Healthcare Materials* 14 (2025): 2403570, https://doi.org/10.1002/adhm.202403570.

47. T. T. D. Pham, S. J. Jung, C. M. Oh, et al., "Conjugated Polymer Nanoparticles: Photothermal and Photodynamic Capabilities According to Molecular Ordering in Their Assembly Structures," *Macromolecules* 56 (2023): 311–322, https://doi.org/10.1021/acs.macromol.2c01815.

48. Z. H. Sheng, D. H. Hu, M. B. Zheng, et al., "Smart Human Serum Albumin-Indocyanine Green Nanoparticles Generated by Programmed Assembly for Dual-Modal Imaging-Guided Cancer Synergistic Phototherapy," *Acs Nano* 8 (2014): 12310–12322, https://doi.org/10.1021/nn5062386.

49. H. L. Wang, X. X. Li, B. W. C. Tse, et al., "Indocyanine Green-incorporating Nanoparticles for Cancer Theranostics," *Theranostics* 8 (2018): 1227–1242, https://doi.org/10.7150/thno.22872.

50. H. Ji, Z. Zheng, S. Li, et al., "Research Progress of Serum Albumin in the Field of Drug Delivery," *Interdisciplinary Medicine* 2 (2024): 20240010.

21922659, 2026, 15, Downloaded from https://advanced.onlinelibrary.wiley.com/doi/10.1002/adhm.202505692 by Ewha Womans University Library, Wiley Online Library on [28/09/2026]. See the Terms and Conditions (https://onlinelibrary.wiley.com/terms-and-conditions) on Wiley Online Library for rules of use; OA articles are governed by the applicable Creative Commons License

51. W. L. Chen, Z. H. Wang, M. Y. Tian, et al., "Integration of TADF Photosensitizer as "Electron Pump" and BSA as "Electron Reservoir" for Boosting Type I Photodynamic Therapy," *Journal of the American Chemical Society* 145 (2023): 8130–8140, https://doi.org/10.1021/jacs.3c01042.

52. X. Han, R. Wang, X. Song, F. Yu, C. Lv, and L. Chen, "A mitochondrial-targeting Near-infrared Fluorescent Probe for Bioimaging and Evaluating Endogenous Superoxide Anion Changes During Ischemia/Reperfusion Injury," *Biomaterials* 156 (2018): 134–146, https://doi.org/10.1016/j.biomaterials.2017.11.039.

53. X. Song, S. Bai, N. He, et al., *ACS Sensors* 6 (2021): 1228–1239.

Supporting Information

Additional supporting information can be found online in the Supporting Information section.

Supporting File: adhm70881-sup-0001-SuppMat.docx

21922659, 2026, 15, Downloaded from https://advanced.onlinelibrary.wiley.com/doi/10.1002/adhm.202505692 by Ewha Womans University Library, Wiley Online Library on [28/09/2026]. See the Terms and Conditions (https://onlinelibrary.wiley.com/terms-and-conditions) on Wiley Online Library for rules of use; OA articles are governed by the applicable Creative Commons License